Supplementary Information

Lattice Distortion Enabling Enhanced Strength and Plasticity in High Entropy Intermetallic Alloy

H. Wang et al.

Corresponding authors: Y. Yang, yonyang@cityu.edu.hk; C. W. Pao, cwpao@gate.sinica.edu.tw; Y. Liu, yonliu@csu.edu.cn

Supplementary Figures

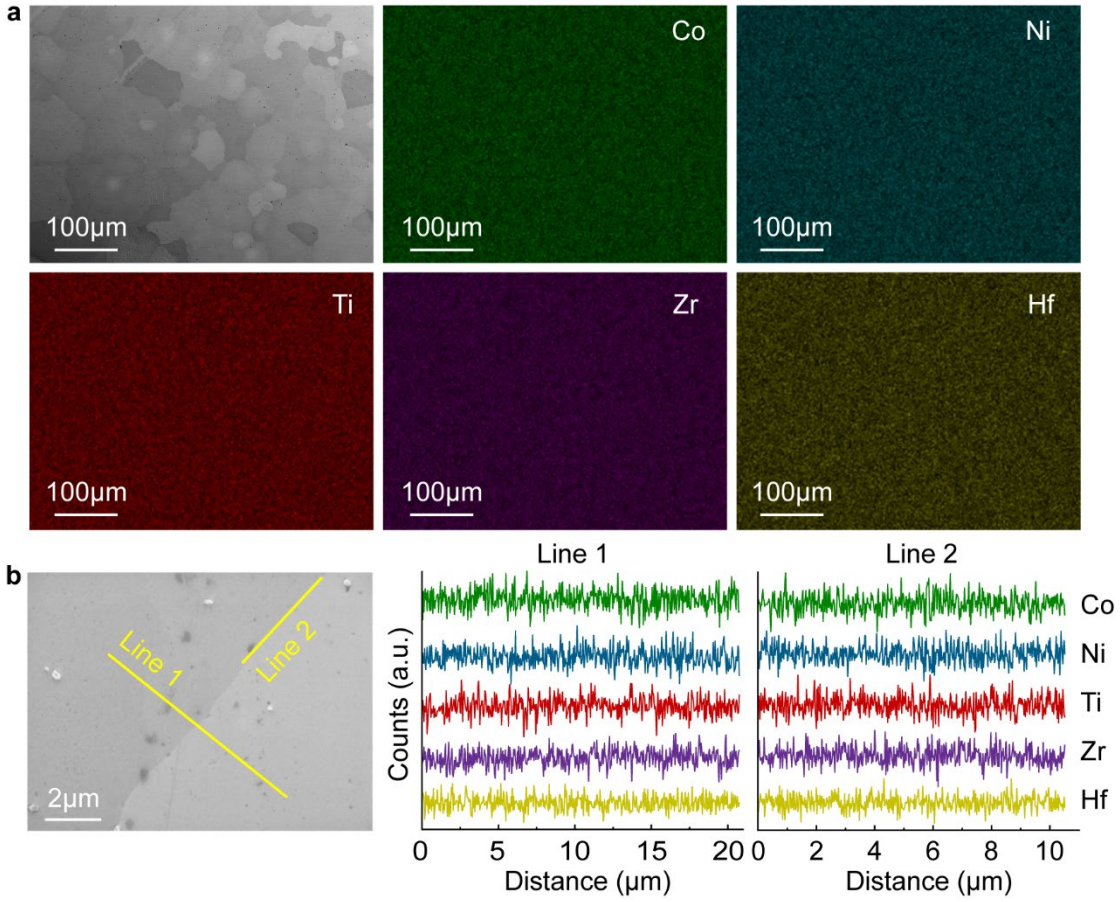

Supplementary Fig.1 Characterization of polycrystalline $(CoNi)_{50}(TiZrHf)_{50}$. a, The backscatter electron image and elemental distributions of $(CoNi)_{50}(TiZrHf)_{50}$. **b**, The elemental distributions across (line 1) and along (line 2) a grain boundary.

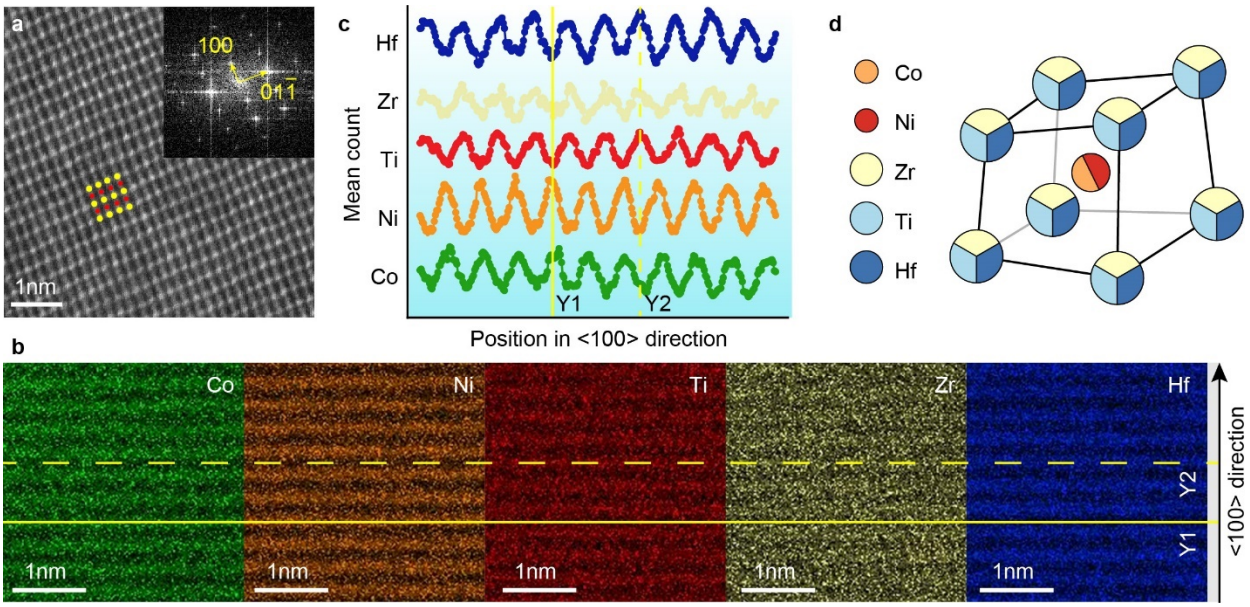

Supplementary Fig. 2 Structure characterization of $(CoNi)_{50}(TiZrHf)_{50}$ alloy. a, The STEM-HAADF image with [011] zone axis, where the red and yellow dots indicate the sites of two sublattices in the B2 lattice. **b,** The elemental mapping obtained by STEM-EDS along the [011] zone axis. **c,** The statistical distribution of elements along <100> direction shown in **b**. **d,** The schematic illustration of the distorted B2 lattice in $(CoNi)_{50}(TiZrHf)_{50}$ according to **a-c**.

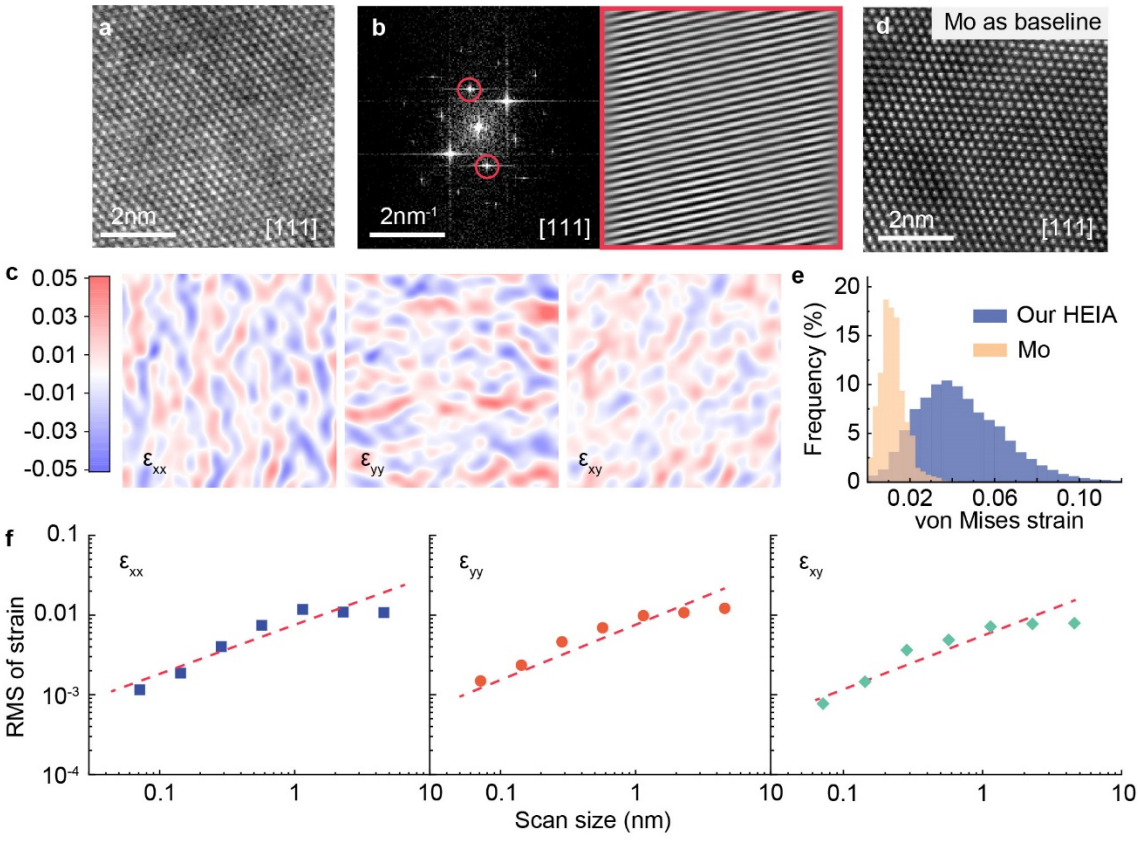

Supplementary Fig. 3 The experimentally mapped lattice strain in $(CoNi)_{50}(TiZrHf)_{50}$. a, The STEM-HAADF image with zone axis [111] shows the region for lattice strain mapping. The filtered inverse FFT image in **b**. indicates that the region is defect free. **c**, The contour maps of the three stain components: ε_{xx}, ε_{yy} and ε_{xy}. **d**, The STEM-HAADF image of elemental metal Mo as a baseline. **e**, The distribution of von Mises strain of our HEIA compared with Mo. **f**, The correlation between the root-mean-square of the strain and the size of "box" within which the strains are measured. Source data are provided as a Source Data file.

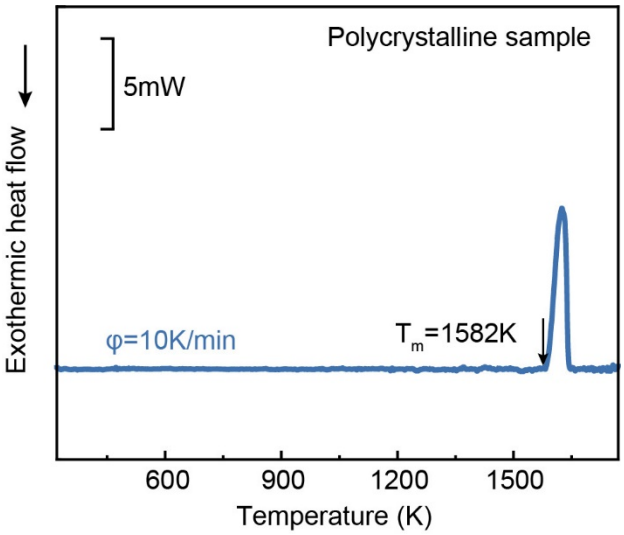

Supplementary Fig. 4 The DSC curve of the polycrystalline $(CoNi)_{50}(TiZrHf)_{50}$ alloy. The heating rate φ is 10 K/min and T_m is the melting temperature.

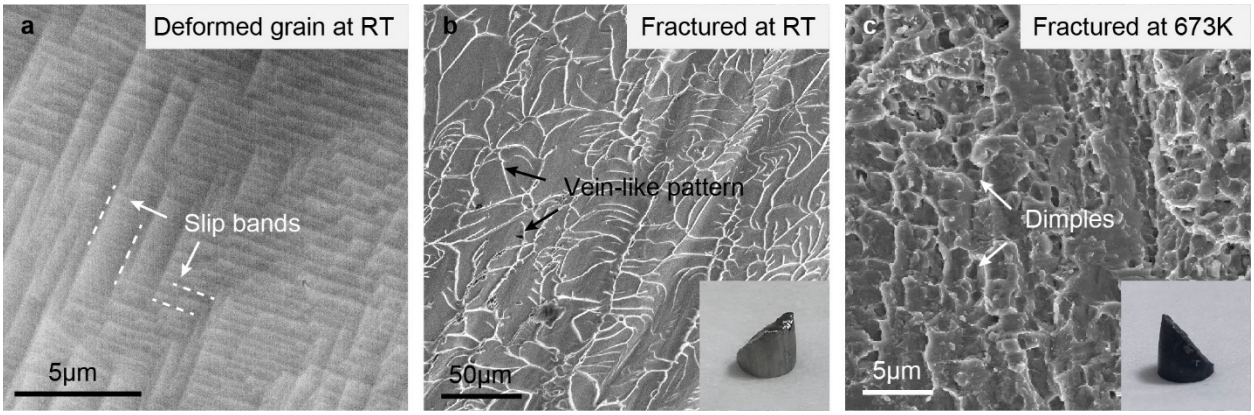

Supplementary Fig. 5 Mechanical properties and microstructures of polycrystalline $(CoNi)_{50}(TiZrHf)_{50}$ alloy. a, The ECCI image of a deformed grain at RT. The SEM images of the fractured surface at RT (**b**) and at 673 K (**c**). The insets are the fracture samples.

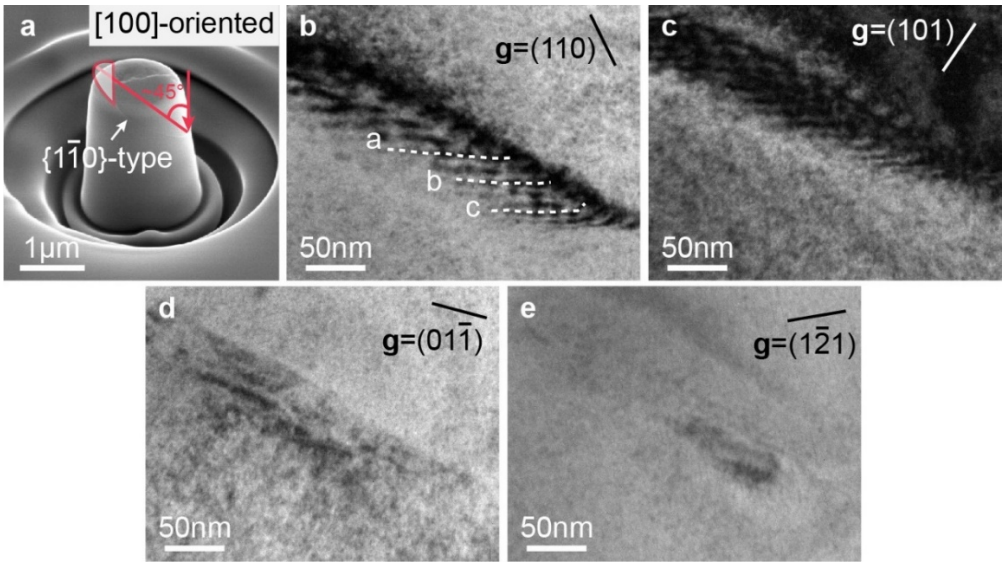

Supplementary Fig. 6 The dislocation structure in the deformed [001] single crystalline sample. a, The SEM image of the deformed sample. According to the angle between the slip plane and loading direction (red arrow), the slip plane was determined to be of a {110} type. The TEM image of the dislocations obtained at $\mathbf{g} = (110)$ and the beam direction $\mathbf{Z} = [\bar{1}11]$ (**b**), $\mathbf{g} = (101)$ and the beam direction $\mathbf{Z} = [\bar{1}11]$ (**c**), $\mathbf{g} = (01\bar{1})$ and the beam direction $\mathbf{Z} = [011]$ (**d**) and $\mathbf{g} = (1\bar{2}1)$ and the beam direction $\mathbf{Z} = [\bar{1}13]$ (**e**). The **g•b**=0 out of contrast analyses indicate that the dislocations are of the <111> type. Please see Supplementary Table 4 for the detailed analyses.

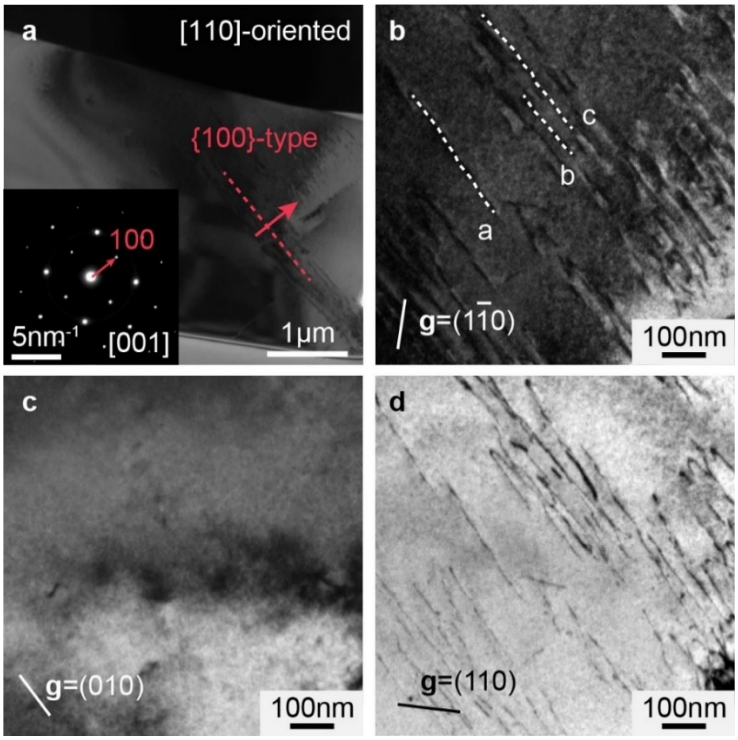

Supplementary Fig. 7 The dislocation structure in the deformed [110] single crystalline sample. a, The TEM image of the deformed sample. The red arrows denote the normal direction of the slip planes, indicative of a {100}-type slip according to the SAED pattern (the inset). The TEM images of the dislocations obtained at $\mathbf{g} = (1\bar{1}0)$ and the beam direction $\mathbf{Z} = [001]$ (**b**), $\mathbf{g} = (010)$ and the beam direction $\mathbf{Z} = [001]$ (**c**) and $\mathbf{g} = (110)$ and the beam direction $\mathbf{Z} = [001]$ (**d**). The **g•b**=0 out of contrast analyses indicate that the dislocations are of the <100> type. Please see Supplementary Table 5 for the detailed analyses.

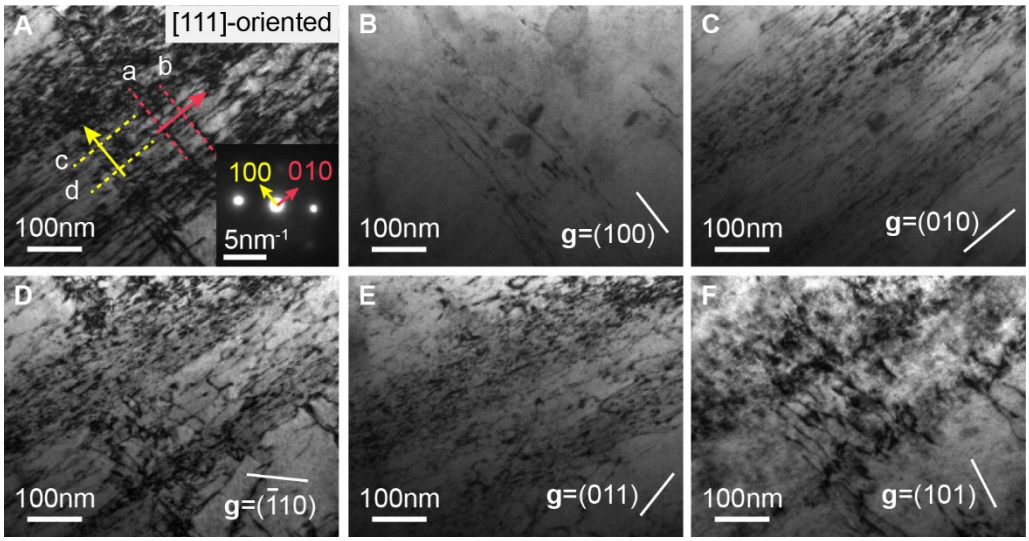

Supplementary Fig. 8 The dislocation structure in the deformed [111] single crystalline sample. a, The TEM image of the deformed sample. The red and yellow arrows represent the normal directions of the two slip planes marked by red and yellow dashed lines, respectively. The inset SAED pattern indicates that both slip planes are of {010} type. The TEM images of the dislocation structures obtained at $\mathbf{g} = (100)$ and the beam direction $\mathbf{Z} = [001]$ (**b**). $\mathbf{g} = (010)$ and the beam direction $\mathbf{Z} = [001]$ (**c**), $\mathbf{g} = (\bar{1}10)$ and the beam direction $\mathbf{Z} = [11\bar{1}]$ (**d**), $\mathbf{g} = (011)$ and the beam direction $\mathbf{Z} = [11\bar{1}]$ (**e**) and $\mathbf{g} = (101)$ and the beam direction $\mathbf{Z} = [11\bar{1}]$ (**f**). The **g•b**=0 out of contrast analyses indicate that the dislocations are of the <100> type. Please see Supplementary Table 6 for the detailed analyses. [Adapted with permission from the Ref.[1]].

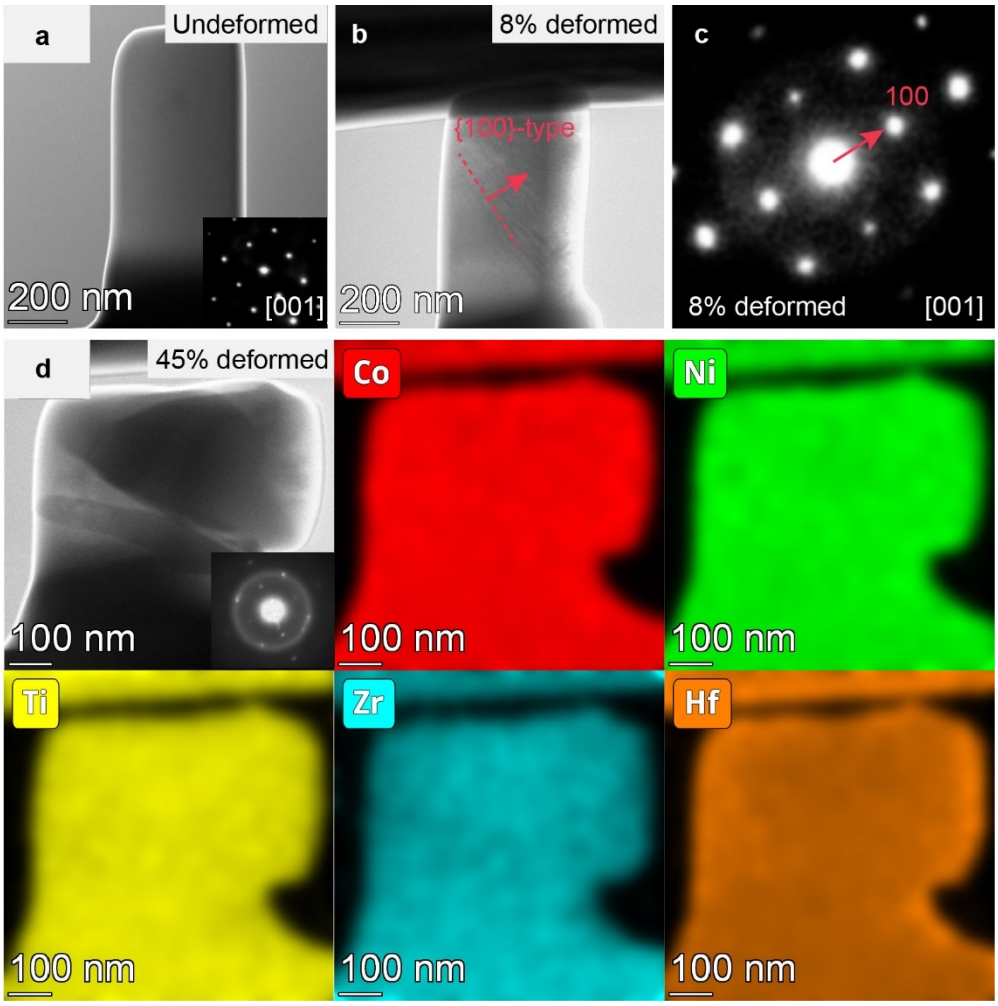

Supplementary Fig. 9 The in-situ compression on $(CoNi)_{50}(TiZrHf)_{50}$ at room temperature. **a,** The ABF-STEM image of the sample before deformation. The inset is the SAED pattern with zone axis [001]. **b,** The TEM image of the deformed sample with strain of 8%. The red arrow denotes the normal direction of the slip planes, which is determined to be of type {100} according to the SAED pattern in **c**. **d,** The elemental mapping of the highly deformed sample with strain of 45%. The inset SAED pattern indicates the formation of an amorphous phase.

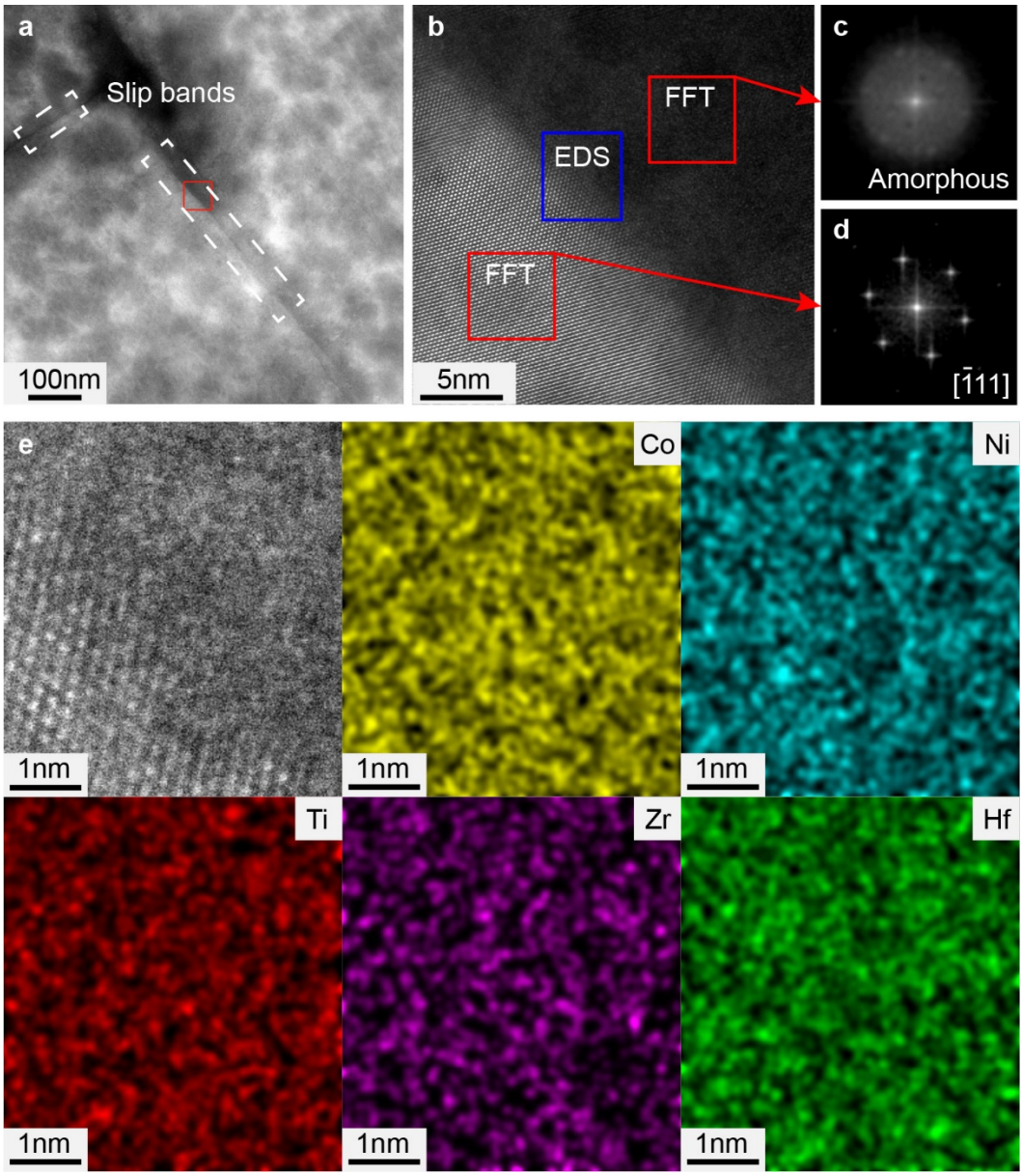

Supplementary Fig. 10 Structural characterization of polycrystalline $(CoNi)_{50}(TiZrHf)_{50}$ after deformation. **a,** The HAADF-STEM image of the sample after deformation. The white dotted box highlights slip bands. **b,** The enlarged image of the red-boxed area in **a**, inside which the amorphous phase can be observed. The amorphous and crystal structures are characterized through FFT, as shown in **c** and **d**, respectively. **e,** The elemental mapping of the blue-boxed area in **b**.

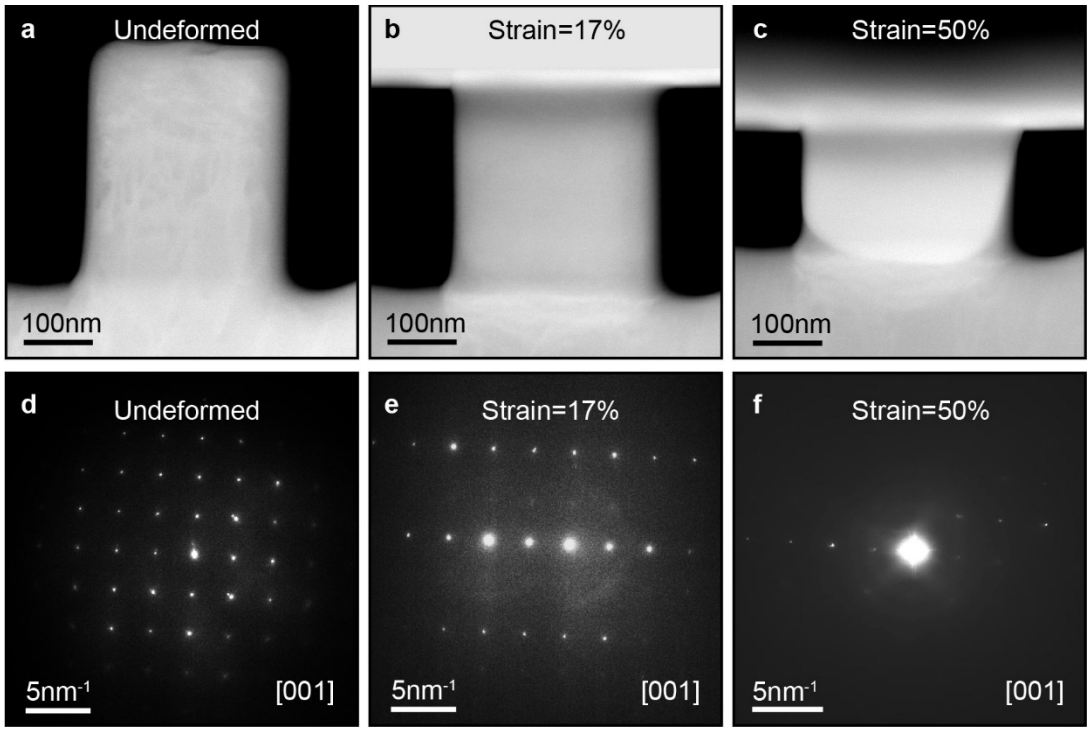

Supplementary Fig. 11 The in-situ compression on $(CoNi)_{50}(TiZrHf)_{50}$ at 573K. The LAADF-STEM images of the sample before deformation (**a**), with strain of 17% (**b**) and 50% (**c**). The SAED patterns with zone axis [001] of sample before deformation (**d**), with strain of 17% (**e**) and 50% (**f**).

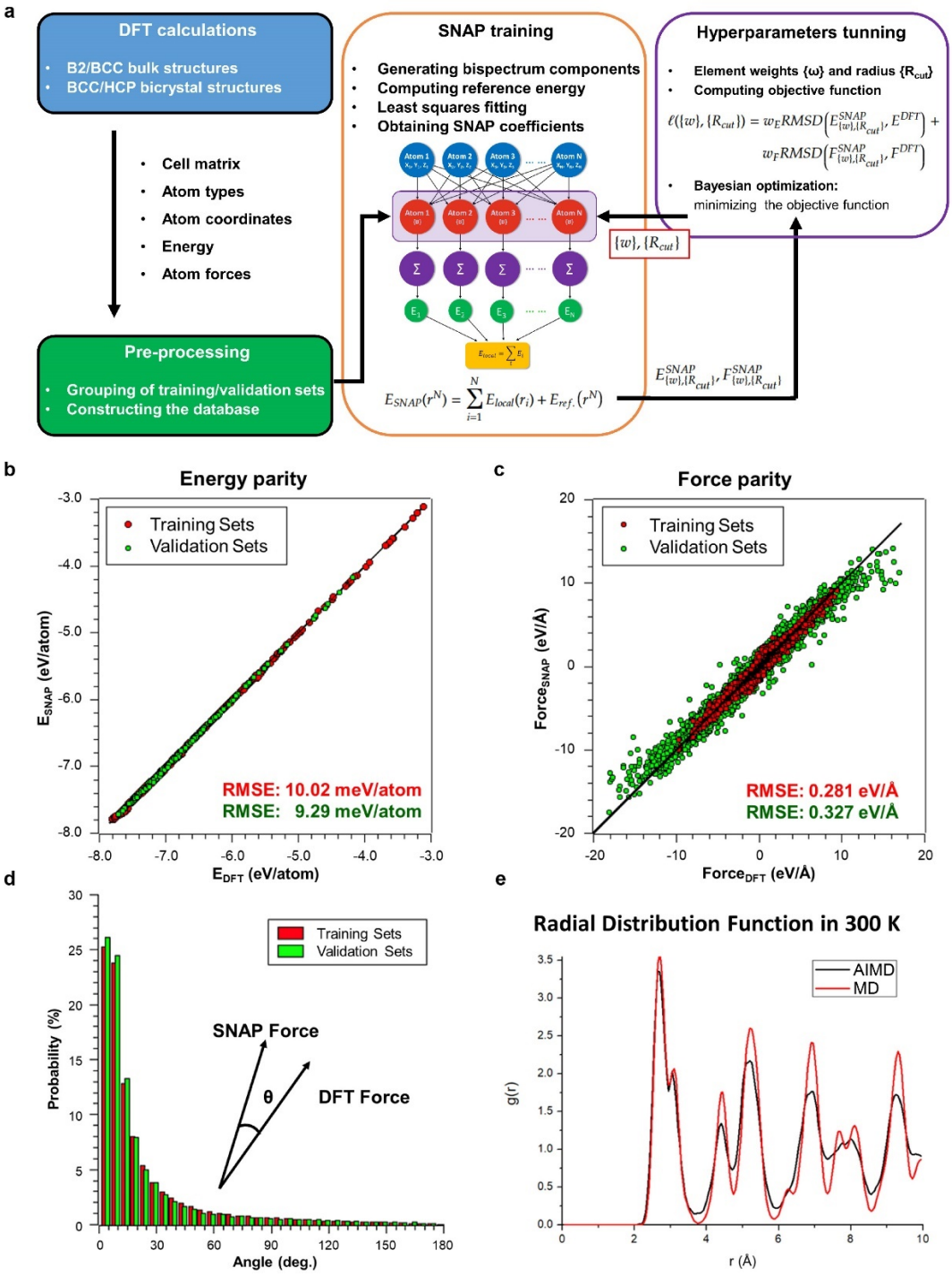

Supplementary Fig. 12 Parameterization of SNAP potential. a, The training work flow of SNAP potential. The parity plot of the energy (**b**), atomic force magnitude (**c**) and distribution of the error of force direction between DFT and SNAP for both training and validation sets (**d**). **e,** The radial distribution function (RDF) of B2 bulk equilibrated structures of $(CoNi)_{50}(TiZrHf)_{50}$ that illustrated from AIMD and classical MD combined with SNAP model.

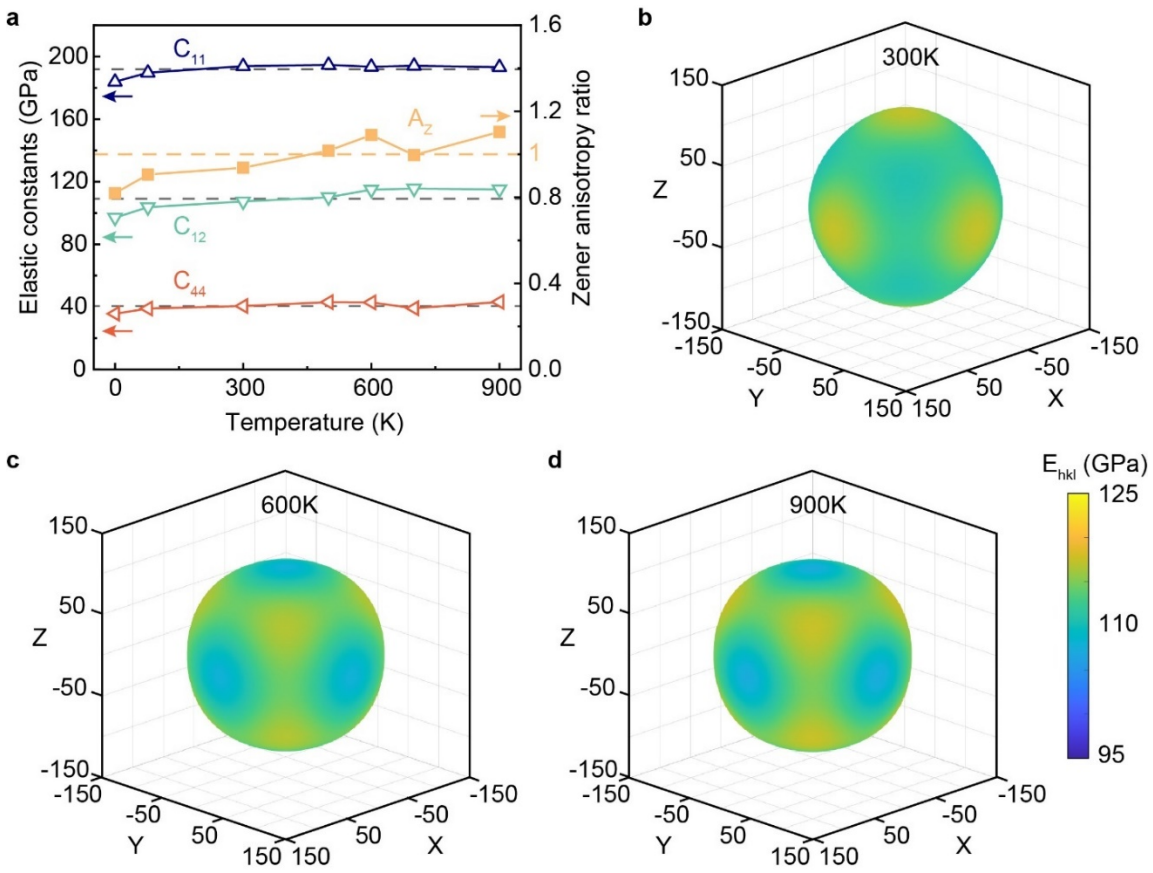

Supplementary Fig. 13 Elastic properties of $(CoNi)_{50}(TiZrHf)_{50}$ at different temperatures. a, Elastic constants (C_{11}, C_{12} and C_{44}) and Zener anisotropy ratio versus temperature. **b-d,** The contour maps of elastic modulus E_{hkl} for the $(CoNi)_{50}(TiZrHf)_{50}$ at 300 K, 600 K and 900 K, respectively.

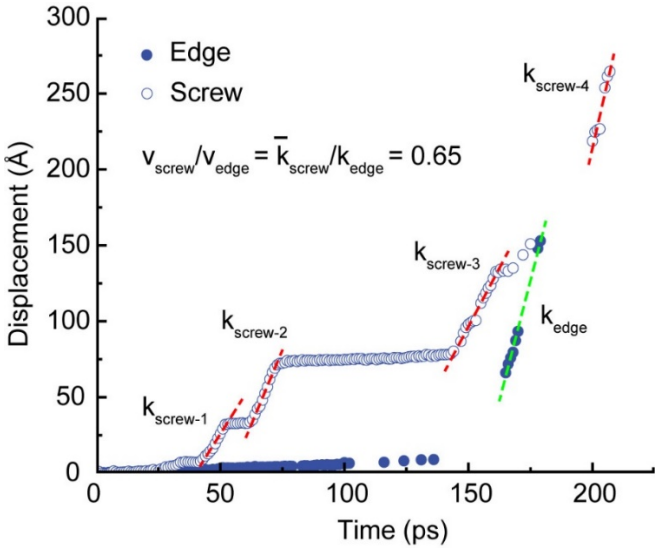

Supplementary Fig. 14 The displacement of screw and edge dislocations as a function of time at 300 K. The velocity (v) is measured as the average slope (k) of fitted lines. Source data are provided as a Source Data file.

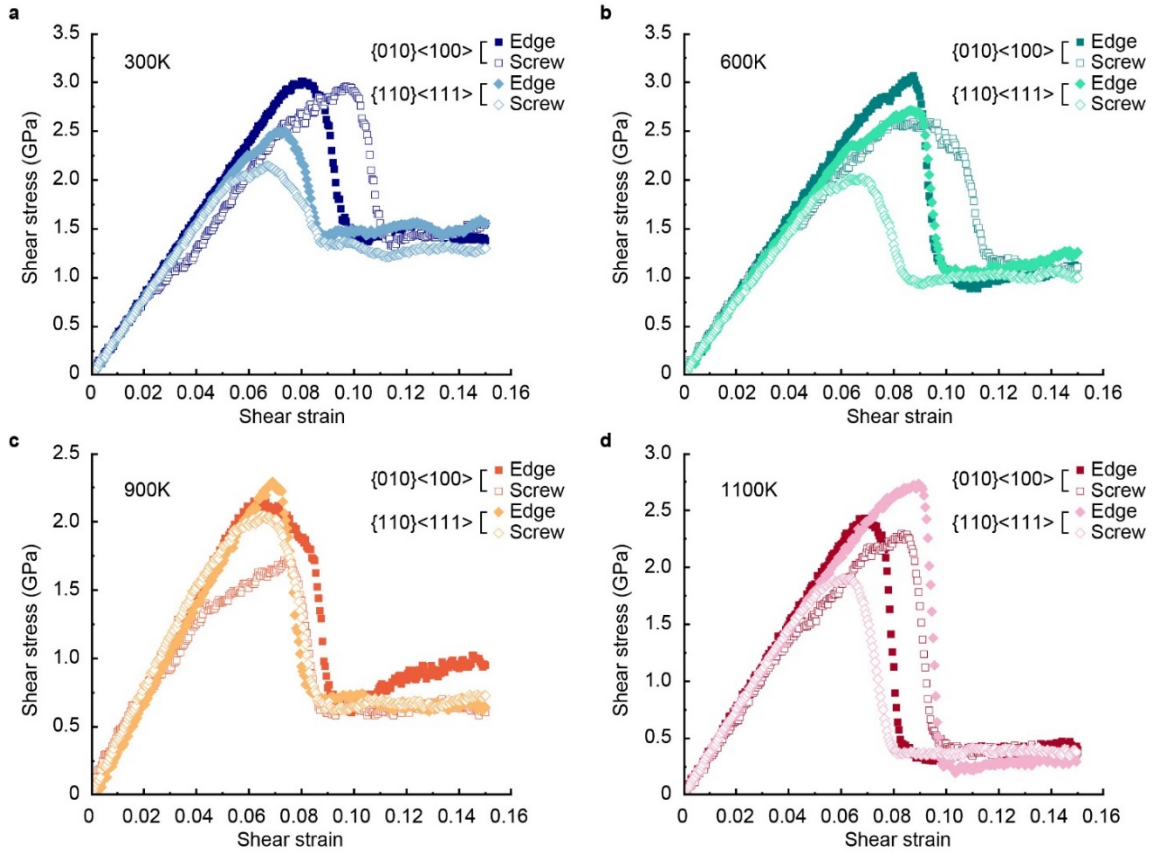

Supplementary Fig. 15 The temperature-dependent shear stress-strain curves obtained in MD models at different temperatures. a-d, 300 K, 600 K, 900 K and 1100 K, respectively. Note that the high peak stress in **d** is mainly caused by the different fixed layer condition during equilibrium relaxation simulation, which is completely unrelaxed at 1100 K in order to avoid its pre-melting. Source data are provided as a Source Data file.

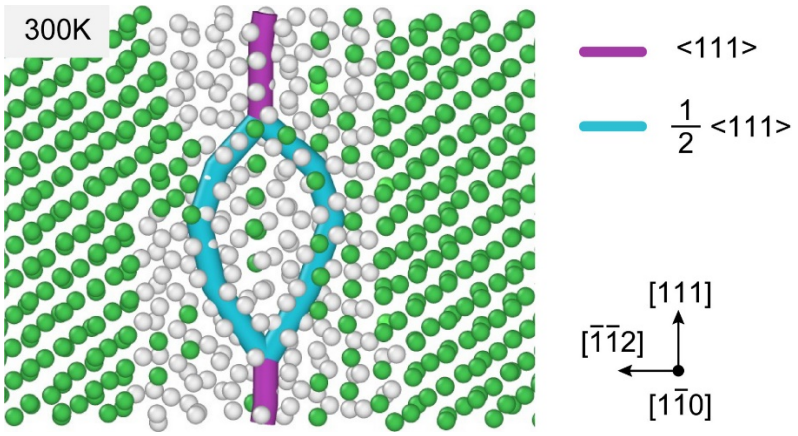

Supplementary Fig. 16 Dissociation of {110}<111> dislocation. Here green and grey balls represent atoms with B2 and non-B2 packing respectively.

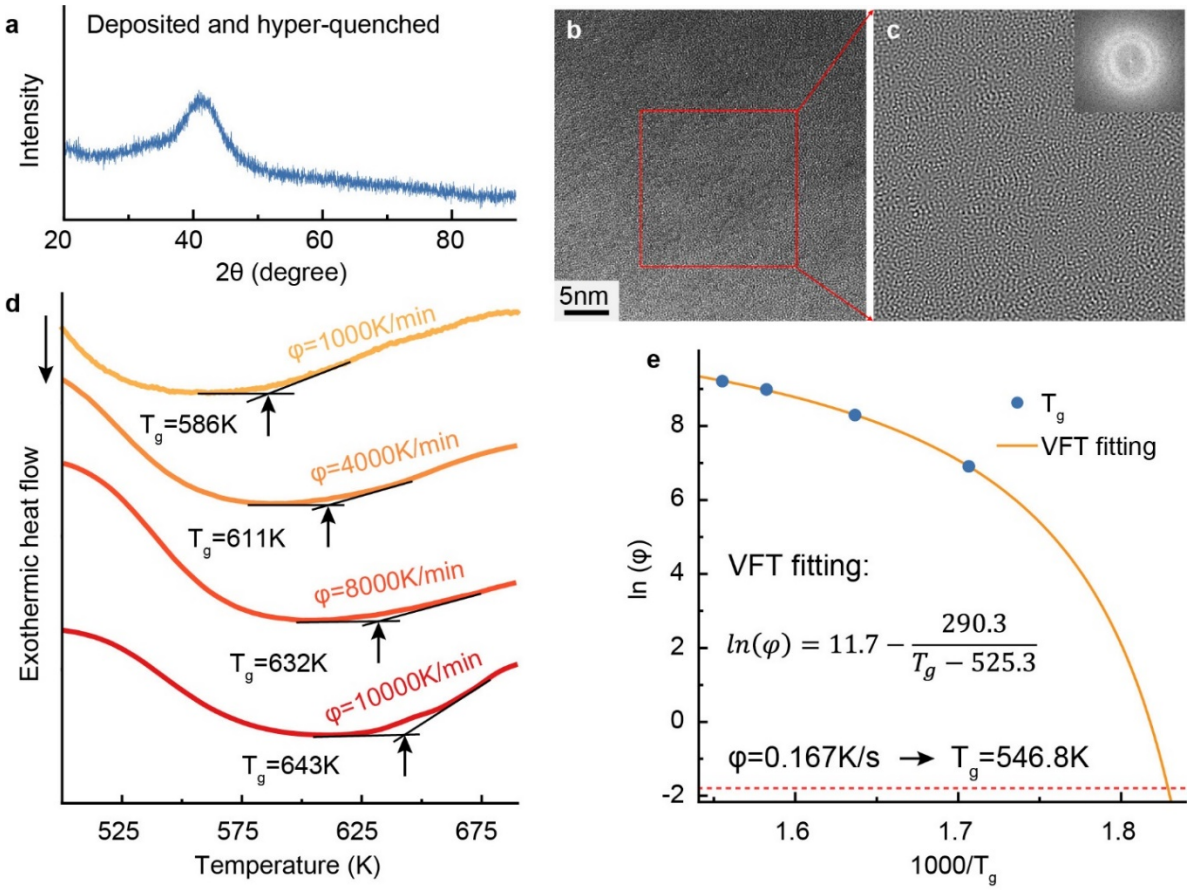

Supplementary Fig. 17 Structure and thermal characterization of the hyper-quenched amorphous $(CoNi)_{50}(TiZrHf)_{50}$. a, The XRD pattern of the deposited and hyper-quenched $(CoNi)_{50}(TiZrHf)_{50}$ thin film. **b,** The HRTEM image of amorphous $(CoNi)_{50}(TiZrHf)_{50}$. **c,** The enlarged image of the red-boxed area in **b**. The inset is FFT image. **d,** The flash DSC results of the

$(CoNi)_{50}(TiZrHf)_{50}$ thin film obtained at different heating rates (φ). T_g is glass transition temperature. **e,** The VFT fitting of heating rate versus glass transition temperature.

Supplementary Tables

Supplementary Table 1. A summary of the yield strengths measured for BCC RMEAs/RHEAs, BCC conventional alloys, B2 conventional alloys, BCC elemental metals and $(CoNi)_{50}(TiZrHf)_{50}$ at different temperatures. Note that the data of yield strength were obtained by compression tests, except for those of Ta, Mo and W that were obtained by tensile tests. The melting temperature of the alloys or elemental metals is obtained as follows: [a] CALPHAD calculations with the TCHEA3 database according to Ref.[2], [b] CALPHAD calculations with the TCHEA5 database, [c] Binary phase diagrams, [d] CALPHAD calculations with the SGTE database, and [e] Experiments.

Composition	Structure	T_m (K)	T (K)	σ_y (MPa)	Ref.
AlNbTiV	BCC	2153[a]	298	1020	3
			873	810	
			1073	685	
			1273	158	
AlCrMoTi	BCC	2149[a]	673	1069	4
			873	1025	
			1073	891	
			1273	374	
$AlCr_{0.5}NbTiV$	BCC	1962[a]	298	1300	5
			873	1005	
			1073	640	
			1273	40	
$Al_{0.4}Hf_{0.6}NbTaTiZr$	BCC	2021[a]	298	1841	6
			1073	796	
			1273	298	
			1473	89	
CrMoNbV	BCC	2174[b]	298	1497	7
			573	1415	
			773	1254	
			973	1156	
			1073	1100	

			1173	1066	
			1273	1057	
HfNbTaTiZr	BCC	2124[a]	298	929	[8]
			673	790	[9]
			873	675	
			1073	535	
			1273	295	
			1473	92	
HfMoTaTiZr	BCC	2066[a]	298	1600	[10]
			1073	1045	
			1273	855	
			1473	404	
HfMoNbTiZr	BCC	2040[a]	298	1575	[11]
			1073	825	
			1173	728	
			1273	635	
			1373	397	
			1473	187	
HfMoNbTaTiZr	BCC	2113[a]	298	1512	[10]
			1073	1007	
			1273	814	
			1473	556	
MoNbTaW	BCC	3077[a]	298	1058	[12]
			873	561	
			1073	552	
			1273	548	
			1473	506	
			1673	421	
			1873	405	
MoNbTaWV	BCC	2839[a]	298	1246	[12]
			873	862	

			1073	846	
			1273	842	
			1473	735	
			1673	656	
			1873	477	
MoNbTaTiW	BCC	2689[a]	298	1343	[13]
			873	689	
			1073	674	
			1273	620	
			1473	586	
MoNbTaWVTi	BCC	2569[a]	298	1515	[13]
			873	973	
			1073	791	
			1273	753	
			1473	659	
$Ta_{90}W_{10}$	BCC	3317[c]	300	435	[14]
			400	352	
			573	300	
			723	230	
			900	200	
			1050	191	
			1223	160	
$Nb_{73.5}Ti_{18.1}W_{8.4}$	BCC	2698[d]	296	849	[15]
			873	420	
			1073	389	
			1273	348	
			1473	194	
$Nb_{73}Mo_{9.2}Ti_{17.8}$	BCC	2639[d]	296	521	[15]
			873	230	
			1073	207	
			1273	170	

			1473	97	
FeAl	B2	1529[c]	300	799	[16]
			400	728	
			500	712	
			550	699	
			600	651	
			650	581	
			700	449	
			750	369	
			800	304	
NiAl	B2	1911[c]	300	417	[17]
			673	309	
			1073	85	
			1273	59	
CoTi	B2	1600[c]	300	334	[18]
			473	499	
			573	591	
			673	514	
			773	438	
			873	341	
			973	104	
			1073	84	
CoZr	B2	1643[c]	300	138	[19]
			473	181	
			573	246	
			673	241	
			773	215	
			873	155	
			973	96	
$Co_{49.7}Hf_{50.3}$	B2	1913[c]	300	315	[20]
			473	270	

			573	287	
			673	294	
			773	393	
			873	331	
			973	257	
			1073	151	
$(CoNi)_{50}(TiZrHf)_{50}$	B2	1582[e]	298	1538±27	This work
			673	1308±25	
			873	1067±4	
			1073	564±27	
			1273	238±33	
			1423	101±27	

Supplementary Table 2. The detail information of the BCC and B2 alloys in Fig. 1D. The melting temperature of the alloys is obtained as follows: [a] CALPHAD calculations with the TCHEA5 database. [b] CALPHAD calculations with the TCHEA3 database according to Ref.[2]. [c] CALPHAD calculations with the SGTE database. [d] Binary phase diagrams. [e] CALPHAD calculations with the TTTi database.

Composition	**Structure**	**T_m (K)**	**Ref.**
CrMoNbV	BCC	2174[a]	[7]
HfMoNbTaTiZr	BCC	2113[b]	[10]
HfMoTaTiZr	BCC	2066[b]	[10]
MoNbTaWV	BCC	2839[b]	[12]
MoNbTaTiVW	BCC	2569[b]	[13]
MoNbTaTiW	BCC	2689[b]	[13]
$Nb_{71.7}W_{5.9}Hf_{22.4}$	BCC	2748[c]	[15]
$Fe_{60}Al_{40}$	B2	1648[d]	[21]
$Ni_{47}Al_{53}$	B2	1889[d]	[22]
$Ti_{50}Mo_{25}Al_{25}$	B2	2054[e]	[23]
$(FeCoNiCu)_{50}(TiZrHf)_{50}$	B2	1270[a]	[24]

Supplementary Table 3. A summary of the mechanical properties of single crystal $(CoNi)_{50}(TiZrHf)_{50}$. The Young's modulus (E) was measured after the correction of the sample geometry and base effects according to the Ref. [25]. Under the same experimental conditions, different values of σ_y and E came from different micropillars.

Orientation	T (K)	σ_y (MPa)		E (GPa)		Observed slip system	CRSS (MPa)	
[001]	295	3117	3025±95	96	96±1	{110}⟨111⟩	1272	1235±39
		2927		97			1195	
		3031		95			1237	
[101]	295	2889	2792±113	91	92±3	{010}⟨100⟩	1444	1176±245
		2667		95			1333	
		2819		90			1409	
[111]	295	2881	2870±121	90	92±2	{010}⟨100⟩	960	
		2985		93			995	
		2743		93			914	
[111]	423	2442	2539±137	87	90±4	-	-	
		2636		93				
[111]	473	2478	2362±101	99	98±10	-	-	
		2291		87				
		2318		107				
[111]	523	2322	2095±199	95	100±4	-	-	
		2009		102				
		1953		103				
[111]	573	1760	1923±244	103	97±8	-	-	
		1981		99				
		2028		88				

Supplementary Table 4. The **g•b**=0 extinction condition analysis of the dislocations marked in Supplementary Fig. S6. The letters "V" and "I" in the following table represent "visible" and "invisible" respectively.

Zone axis	g	Dislocations		
		a	b	c

$[\bar{1}11]$	(110)	V	V	V
$[\bar{1}11]$	(101)	V	V	V
[011]	$(01\bar{1})$	I	I	I
$[\bar{1}13]$	$(1\bar{2}1)$	I	I	I
Possible Burgers vector		[111] or $[\bar{1}\bar{1}\bar{1}]$		

Supplementary Table 5. The **g•b**=0 extinction condition analysis of the dislocations marked in Supplementary Fig. S7. The letters "V" and "I" in the following table represent "visible" and "invisible" respectively.

Zone axis	**g**	**Dislocations**		
		a	**b**	**c**
[001]	$(1\bar{1}0)$	V	V	V
[001]	(010)	I	I	I
[001]	(110)	V	V	V
Possible Burgers vector		[100] or $[\bar{1}00]$		

Supplementary Table 6. The **g•b**=0 extinction condition analysis of the dislocations marked in Supplementary Fig. S8. The letters "V" and "I" in the following table represent "visible" and "invisible" respectively.

Zone axis	**g**	**Dislocations**			
		a	**b**	**c**	**d**
[001]	(100)	V	V	I	I
[001]	(010)	I	I	V	V
$[11\bar{1}]$	$(\bar{1}10)$	V	V	V	V
$[11\bar{1}]$	(011)	I	I	V	V
$[11\bar{1}]$	(101)	V	V	I	I

Possible Burgers vector	$[100]$ or $[\bar{1}00]$	$[010]$ or $[0\bar{1}0]$

Supplementary References

1. He, Q. F. *et al.* A highly distorted ultraelastic chemically complex Elinvar alloy. *Nature* **602**, 251–257 (2022).

2. Senkov, O. N., Gorsse, S. & Miracle, D. B. High temperature strength of refractory complex concentrated alloys. *Acta Mater.* **175**, 394–405 (2019).

3. Stepanov, N. D., Shaysultanov, D. G., Salishchev, G. A. & Tikhonovsky, M. A. Structure and mechanical properties of a light-weight AlNbTiV high entropy alloy. *Mater. Lett.* **142**, 153–155 (2015).

4. Chen, H. *et al.* Contribution of Lattice Distortion to Solid Solution Strengthening in a Series of Refractory High Entropy Alloys. *Metall. Mater. Trans. A Phys. Metall. Mater. Sci.* **49**, 772–781 (2018).

5. Stepanov, N. D., Yurchenko, N. Y., Skibin, D. V., Tikhonovsky, M. A. & Salishchev, G. A. Structure and mechanical properties of the AlCrxNbTiV (x = 0, 0.5, 1, 1.5) high entropy alloys. *J. Alloys Compd.* **652**, 266–280 (2015).

6. Senkov, O. N., Senkova, S. V. & Woodward, C. Effect of aluminum on the microstructure and properties of two refractory high-entropy alloys. *Acta Mater.* **68**, 214–228 (2014).

7. Feng, R. *et al.* Superior High-Temperature Strength in a Supersaturated Refractory High-Entropy Alloy. *Adv. Mater.* **33**, 2102401 (2021).

8. Senkov, O. N., Scott, J. M., Senkova, S. V., Miracle, D. B. & Woodward, C. F. Microstructure and room temperature properties of a high-entropy TaNbHfZrTi alloy. *J. Alloys Compd.* **509**, 6043–6048 (2011).

9. Senkov, O. N. *et al.* Microstructure and elevated temperature properties of a refractory TaNbHfZrTi alloy. *J. Mater. Sci.* **47**, 4062–4074 (2012).

10. Juan, C. C. *et al.* Enhanced mechanical properties of HfMoTaTiZr and HfMoNbTaTiZr refractory high-entropy alloys. *Intermetallics* **62**, 76–83 (2015).

11. Sheikh, S. *et al.* Alloy design for intrinsically ductile refractory high-entropy alloys. *J. Appl. Phys.* **120**, 164902 (2016).

12. Senkov, O. N., Wilks, G. B., Scott, J. M. & Miracle, D. B. Mechanical properties of Nb25Mo25Ta25W25 and V20Nb20Mo20Ta20W20 refractory high entropy alloys. *Intermetallics* **19**, 698–706 (2011).

13. Han, Z. D. *et al.* Effect of Ti additions on mechanical properties of NbMoTaW and VNbMoTaW refractory high entropy alloys. *Intermetallics* **84**, 153–157 (2017).

14. Lassila, D. H., Goldberg, A. & Becker, R. The effect of grain boundaries on the athermal stress of tantalum and tantalum-tungsten alloys. *Metall. Mater. Trans. A* **33**, 3457–3464 (2002).

15. Senkov, O. N., Rao, S. I., Butler, T. M. & Chaput, K. J. Ductile Nb alloys with reduced density and cost. *J. Alloys Compd.* **808**, 151685 (2019).

16. Baker, I. & Yang, Y. On the yield stress anomaly in stoichiometric FeAl. *Mater. Sci. Eng. A* **239**–**240**, 109–117 (1997).

17. Sheng, L. *et al.* Effect of Au addition on the microstructure and mechanical properties of NiAl intermetallic compound. *Intermetallics* **18**, 740–744 (2010).

18. Takasugi, T. & Izumi, O. Deformation of CoTi polycrystals. *J. Mater. Sci.* **23**, 1265–1273 (1988).

19. Nakamura, M. & Sakka, Y. Compressive deformation of CoZr and (Co,Ni)Zr intermetallic compounds with B2 structure. *J. Mater. Sci.* **23**, 4041–4048 (1988).

20. Takasugi, T., Izumi, O. & Yoshida, M. Anomalous temperature dependence of the yield strength in IVa-VIII intermetallic compounds with B2 structure. *J. Mater. Sci.* **26**, 2941–2948 (1991).

21. Calonne, O., Fraczkiewicz, A. & Louchet, F. Yield strength anomaly in b2-ordered FeAl alloys: role of boron. *Scr. Mater.* **43**, 69–75 (2000).

22. Pascoe, R. T. & Newey, C. W. A. A. The Mechanical Behaviour of the Intermediate Phase NiAl. *Met. Sci. J.* **2**, 138–143 (1968).

23. Lu, Y., Yamada, J., Miyata, R., Kato, H. & Yoshimi, K. High-temperature mechanical behavior of B2-ordered Ti–Mo–Al alloys. *Intermetallics* **117**, 106675 (2020).

24. Yao, K. *et al.* High-entropy intermetallic compound with ultra-high strength and thermal stability. *Scr. Mater.* **194**, 113674 (2021).

25. Yang, Y., Ye, J. C., Lu, J., Liu, F. X. & Liaw, P. K. Effects of specimen geometry and base material on the mechanical behavior of focused-ion-beam-fabricated metallic-glass micropillars. *Acta Mater.* **57**, 1613–1623 (2009).